Case study on using the sliding-LRB system with SMA devices for seismic protection of continuous bridges

Wenzhi Zheng[1], Hao Wang[2], Hong Hao[3], and Kaiming Bi[4]

1. PhD student, Key Laboratory of C & PC Structures of Ministry of Education, Southeast University, Nanjing 210096, China; Centre for Infrastructure Monitoring and Protection, School of Civil and Mechanical Engineering, Curtin University, Bentley, WA 6102, Australia. Email: wzzheng@seu.edu.cn

2. Professor, Key Laboratory of C & PC Structures of Ministry of Education, Southeast University, Nanjing 210096, China. Email: wanghao1980@seu.edu.cn

3. John Curtin Distinguished Professor, Centre for Infrastructure Monitoring and Protection, School of Civil and Mechanical Engineering, Curtin University, Bentley, WA 6102, Australia. Email: hong.hao@curtin.edu.au

4. Senior Lecturer, Centre for Infrastructure Monitoring and Protection, School of Civil and Mechanical Engineering, Curtin University, Bentley, WA 6102, Australia. Email: kaiming.bi@curtin.edu.au

Abstract

The sliding-lead rubber bearing is developed to accommodate the thermal-induced movements of the bridge superstructure. However, compared to the conventional lead rubber bearing, larger residual displacement can be introduced by the sliding-lead rubber bearing and the peak displacement also increases obviously under earthquake ground motions, which need to be avoided in engineering practices. In the present study, shape memory alloy (SMA) devices are introduced to the sliding-lead rubber bearing system to improve the seismic performances of this system. A three-span continuous bridge is selected to conduct the case study, and the seismic responses of the bridge supported by the sliding-lead rubber bearing system with and without SMA devices are calculated and compared.

Keywords: continuous bridge; sliding lead rubber bearing; SMA device; seismic responses

1. INTRODUCTION

Significant bearing movements have been observed in the continuous bridges because of the thermal-induced movement of the bridge superstructure. For example, the bearing movement of Sutton Creek Bridge reached 7.6mm in a daily temperature cycle (Moorty and Roeder 1992). The three-day continuous monitoring carried out by Kromanis et al. (2016) revealed that bearing movements of a continuous box-girder bridge reached almost 80mm by shrinkage. Due to the low stiffness of lead rubber bearings (LRBs), the bearing movements, i.e. the initial displacements to the LRBs can significantly impact the responses of the continuous bridge (Wang et al. 2019). Xing et al. (2012) conducted compression-shear tests to investigate the hysteretic behavior of the sliding-lead rubber bearing (Sliding-LRB), in which the sliding device can accommodate the bearing movements to mitigate its influence on the LRB performance. However, the sliding system provided very limited re-centering capability (Ozbulut and Hurlebaus 2011). Large residual displacements thus are introduced to the structure (Cardone and Gesualdi 2017), which significantly influences the post-quake rescue activities. Furthermore, the near-fault earthquakes with velocity pulses can introduce devastating responses to the isolated structures compared to the far-fault ground motions with equal or larger peak ground acceleration (Loh et al. 2002). It is well known that the superelasticity of shape memory alloys (SMAs) shows promising prospects of recovering the deformations sustained by the structure (Wilson and Wesolowsky 2005; Li et al. 2017). Several studies have shown the effectiveness of the SMA devices fabricated by SMA wires as a re-centering or damping member for response control of bridges (Andrawes and DesRoches 2007, Zhang and Zhu 2007, Dezfuli and Alam 2013, Soul and Yawny 2017, Zheng et al. 2019). Results show that SMAs can provide reliable re-centering capability for reducing the residual deformations of structures and structural elements.

In order to reduce the residual displacement introduced by the sliding-LRBs, SMA devices are introduced into the sliding-LRB system in the present study. A three-span continuous concrete bridge is selected as an example to conduct the case study. Through comparison with the responses of the bridge isolated by the sliding-LRB system, the effectiveness of adding SMA devices into system is examined.

2. A SEISMICALLY ISOLATED BRIDGE

2.1. BRIDGE DESCRIPTION

A three-span continuous isolated bridge with the span lengths of 40m + 64m + 40m is selected for this study (Wang et al. 2019). The superstructure of the bridge is a non-uniform pre-stressed concrete box girder. The substructure consists of four solid reinforced concrete shaft piers. The superstructure is isolated with the sliding-LRB system. The total weight of the superstructure is 78,274.3kN, including live load. The C50 and C35 concrete are employed in constructing the girder and piers, respectively. HRB-400 and HPB-300 steels are used for the longitudinal bars and stirrups of the piers respectively. To reduce the residual displacement, each side of the sliding-LRB is symmetrically arranged two SMA devices, which consist of SMA wires. Fig. 1(a) shows the details of the arrangement. The SMA devices are mainly used to provide re-centering capability for the sliding-LRB system.

2.2. SLIDING-LRB SYSTEM WITH SMA DEVICES

Figs. 1(b) and 1(c) show the force-deformation behaviors of the sliding-LRB system and SMA device. As shown in Fig. 1(b), when the peak displacement of the sliding-

LRB system with SMA devices is less than d_s, which is a value when the displacement of the sliding-LRB system reaches the sliding displacement limit, and can be calculated by Eq.(4), the force provided by the sliding-LRB system with SMA devices can be obtained from Eq. (1)

$$F = \mu \cdot W \cdot z + \sum F_{si} \tag{1}$$

where W is the normal load carried by the sliding surface; μ is the frictional coefficient; z is a hysteretic dimensionless quantity; F_{si} is the level of force provided by the i^{th} SMA device. At sliding velocity v, μ can be approximated as follows

$$\mu = \mu_{max} - (\mu_{max} - \mu_{min}) \cdot e^{-av} \tag{2}$$

where μ_{max} and μ_{min} are the friction coefficient at high velocities and very low velocities, respectively; a is a constant depending on the given pressure, temperature and condition of the interfaces; and z evolves based on Eq. (3) (Constantinou et al. 1990)

$$(\frac{\mu W}{k_e} + d_y) \cdot \dot{z} = A \cdot \dot{d} - \beta_0 \cdot \dot{d} \cdot |z|^{\eta_0} + \gamma_0 \cdot |\dot{d}| \cdot z \cdot |z|^{\eta_0 - 1} \tag{3}$$

where A, β_0, γ_0 and η_0 are dimensionless constants that control the shape of the hysteretic response, which are suggested as: A=1, β_0= 0.1, γ_0 = 0.9 and η_0= 2 by Constantinou et al (1990). As shown in Fig. 1(b), F_y is the friction force of the sliding device, respectively; d_y is the yield displacement of the sliding device and selected as 1mm in the present study (MTPRC 2013); $\dot{d}$ is the relative velocity; d_0 is the sliding displacement limit; k_e is the elastic stiffness of LRB; $d_{y'}$ is the displacement of the sliding-LRB system when the LRB yields; and $F_{y'}$ is the yield force of the sliding-LRB system. d_s can be calculated by Eq. (4)

$$d_s = d_0 + d_y + (\mu \cdot W)/k_e \tag{4}$$

The level of force provided by the i^{th} SMA device in the horizontal direction can be obtained by Eq. (5)

$$F_{si} = \begin{cases} k_{si} u & , u \le u_y \\ k_{si} u_y + \alpha k_{si} (u - u_y) & , u > u_y \end{cases} \tag{5}$$

where k_{si} is the elastic stiffness of the i^{th} SMA device; u_y is the yield displacement; α is the strain hardening ratio during the phase transformation. As shown in Fig. 1(c), the SMA device is represented by an idealized force-deformation relationship. Such a simplification shows minimal impact on the structural response (Andrawes and DesRoches 2007). In Fig. 1(c), β is the ratio of the vertical height of the flag in terms of stress to the phase transformation starting stress, γ is the strain hardening ratio during the martensite phase. When the peak displacement of the sliding-LRB system with SMA devices is larger than d_s, the force-deformation behavior of the sliding-LRB system with SMA devices is updated as

$$F = \sigma_{yL} A_L z' + k_d d' + \sum F_{si} \tag{6}$$

where σ_{yL} is the effective yield stress of the lead core; A_L is the cross section area of the lead core; k_d is the postelastic stiffness of the LRB; z' is a hysteretic dimensionless quantity that evolves based on Eq. (7) (Constantinou and Adnane 1987)

$$(d_{y'} - d_0 - d_y) \cdot \dot{z}' = \left(B - |z'|^2 C \cdot (1 + \mathrm{sgn}(\dot{d}' \cdot z')) \right) \cdot \dot{d}' \tag{7}$$

where B and C are dimensionless quantities that are dependent on the shape and size of the hysteretic loop, the values B = 1 and C = 0.5 suggested by Kalpakidis et al. (2010) are used. The *sgn* denotes the signum function. d' can be obtained by Eq. (8)

$$d' = d - (d_0 + d_y) \tag{8}$$

2.3. NUMERICAL MODEL

The numerical model (Wang et al. 2019) of the three-span continuous bridge shown in Fig. 1 is developed in the *OpenSees* platform (PEERC 2016). The elastic beam

column element is used to model the girders and piers. Linear elastic material is utilized in the model. The flat sliding element is selected to model the hysteretic behavior of the sliding device. The LeadRubberX element is selected to model the hysteretic behavior of the LRB. The tension-compression gap model is selected to simulate the hysteretic behavior of the restrainer and sliding displacement limit, which is assumed as rigid (Bi et al. 2013). The self-centering material model is selected to model the hysteretic behavior of the SMA device. In the numerical simulation, a damping ratio of 2% is assumed.

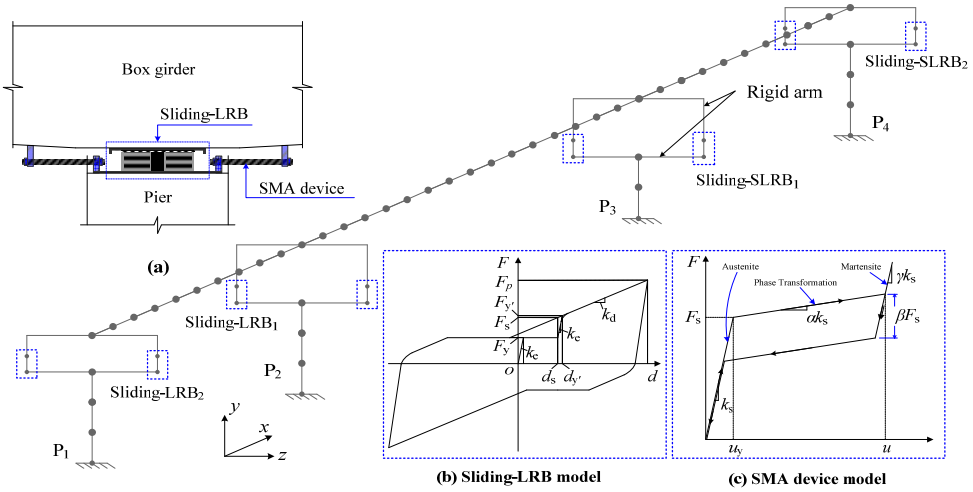

Fig. 1. Elevation view and numerical model of a three-span continuous bridge

3. NUMERICAL RESULTS

3.1. EARTHQUAKE GROUND MOTIONS

In the present study, 45 near-fault records (from Günay and Sucuoğlu 2009) are selected for the time history analyses. Fig. 2 shows the 5% damped pseudo-acceleration response spectra (MTPRC 2008) and scaled mean spectrum of the 45 earthquake ground motions based on the method proposed by ASCE (2005).

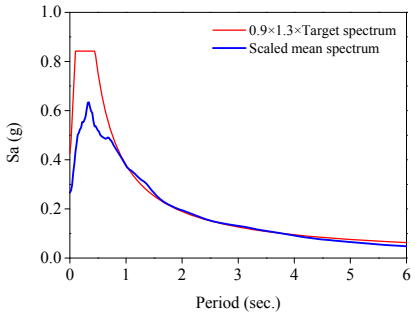

Fig. 2. Target spectrum and scaled mean spectrum (5% damping)

3.2. PARAMETER DESIGN OF SMA DEVICE

In the present study, the values of α and β shown in Fig. 1(c) are assumed as constant for the parametric analysis and equal to 0.05 and 0.4 respectively (Otsuka and Wayman 1999). The sliding displacement limit of the middle bearing is 25mm, and that of the side bearing is selected as 2 times of that of the middle bearing. In order to determine the optimum amount of the SMA wires using in SMA device, the optimum parameter of SMA wires is determined based on the following procedure:

The phase transformation starting force, which represents the total level of force provided by SMA devices, F_s, can be obtained by Eq. (9)

$$F_s = \alpha_s \cdot F_R \tag{9}$$

where α_s is the scaling factor to specify the level of force provided by SMA devices into the sliding-LRB system, and is chosen from 0.1 to 1.0 with the increment of 0.1; F_R is the reference force, which is defined as 10% of the base shear of the middle pier of the reference bridge with sliding-LRB system. In this study, the reference force is selected as 470kN. As suggested by Zheng et al. (2019), the yield displacement of SMA wires is selected as 30mm. A typical strain value of 5% is selected as the strain of the SMA wires at the end of the phase transformation (Soul and Yawny 2017).

The ratio of the amount of the SMA wires in SMA device between the side bearing and middle bearing, β_{sp}, is termed as the distribution ratio in terms of balancing the increment of base forces among the piers. The amount of the SMA wires of the SMA device in the side pier, F_{sp}, can be determined by Eq. (10)

$$F_{sp} = \beta_{sp} \cdot F_s \tag{10}$$

where β_{sp} is selected from 0.0 to 1.0 with the increment of 0.1. The optimal α_s and β_{sp} can be determined when the normalized responses satisfy Eqs. (11) and (12)

$$\max\left\{\Delta R_{d,k+1}, \Delta d_{k+1}\right\} < \min\left\{\Delta R_{d,k}, \Delta d_k\right\} \tag{11}$$

$$\min\left\{\Delta R_{d,k}, \Delta d_k\right\} \le \max\left\{\Delta F_{b,k,l}, \Delta M_{b,k,l}\right\} \tag{12}$$

where $\Delta R_{d,k}$ is the decrement of the normalized residual displacement between k^{th} and $(k+1)^{th}$ scaling factor; Δd_k is the corresponding decrement of the normalized peak displacement. $\Delta F_{b,k,l}$ is the increment of the normalized base shear between the k^{th}, l^{th} and $(k+1)^{th}$ scaling factor, $(l+1)^{th}$ distribution ratio. $\Delta M_{b,k,l}$ is the increment of the normalized base bending moment. Herein the normalized responses are obtained by dividing the peak response of the sliding-LRB system with SMA devices from those of the sliding-LRB system without SMA devices. When the normalized responses satisfy Eqs. (11) and (12), the optimum scaling factor and distribution ratio can be determined.

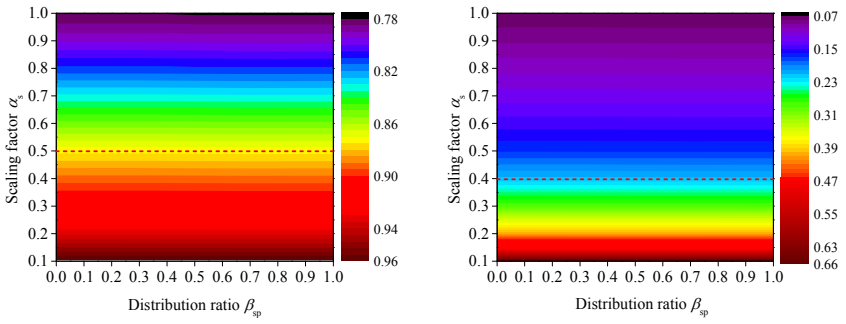

(a) (b)

Fig. 3. Variations of normalized responses: (a) peak displacement; (b) residual displacement

Fig. 3(a) shows the variations of the normalized peak displacement with respect to the scaling factor α_s and distribution ratio β_{sp}. It can be seen that the peak displacement shows a gradual reduction trend with the increase of the scaling factor, whereas no reduction can be observed with the increase of the distribution ratio. This is because the level of force provided by the SMA device directly depends on α_s. When the scaling factor ranges from 0.1 to 0.4 shown in Fig. 3(b), the residual displacement shows a significant reduction. However, the reduction is much less when the scaling factor is larger than 0.4. The distribution ratio shows a much smaller impact on the residual displacement.

Fig. 4(a) shows the variations of the normalized base shear of the middle pier. It can be seen from Fig. 4(a) that the base shear of the middle pier increases rapidly with the increase of scaling factor, whereas it reduces with the increase of the distribution ratio. This is because the force provided by the SMA device distributed to the side piers

increases with the increase of the distribution ratio. When the scaling factor and distribution ratio are selected as the combinations of the values fallen below the red line in Fig. 4(a), the increment of the base shear of the middle pier can be suppressed to be less than 10% of the reference value. Fig. 4(b) shows the variations of the normalized bending moment of the side pier. It can be seen from Fig. 4(b) that the base bending moment of the side pier shows a rapid increasing trend with the increase of the scaling factor and distribution ratio. When the scaling factor and distribution ratio are selected as the combinations of the values fallen below in the red line in Fig. 4(b) , the increment of the base bending moment of the side pier can be limited to be less than 10% of the reference value.

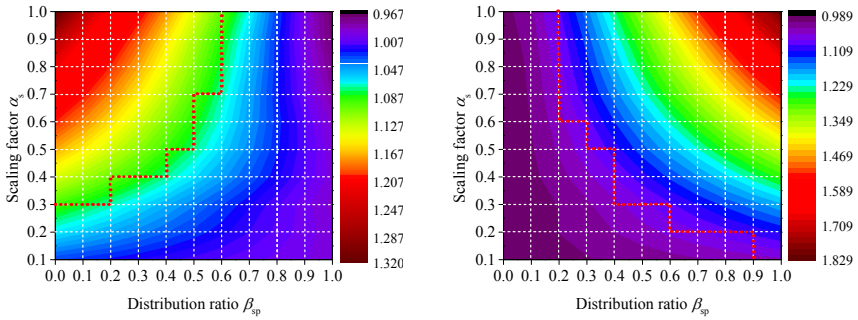

(a) (b)

Fig. 4. Variations of normalized responses: (a) base shear; (b) base bending moment

When the normalized responses satisfy Eqs. (11) and (12), the optimum scaling factor and distribution ratio are determined as 0.3 and 0.6, respectively. Herein the values of μ_{max}, μ_{min} and a at room temperature are approximated from the study of Dolce et al. (2005), as shown in Table 1.

Table 1. The model parameters for sliding surface

Parameter	P (MPa)	μ_{min} (%)	μ_{max} (%)	a (s/mm)
*Sliding-LRB*1	28.1	3.13	10.26	0.022
*Sliding-LRB*2	18.7	4.49	12.7	0.020

3.3. RESULTS

Based on the analysis above, F_s and F_{sp} are equal to 141.0kN and 84.6kN, respectively. For the following analyses, the initial displacements of the sliding segment in middle bearing and side bearing are 13.1mm and 27.4mm (Wang et al. 2019), respectively. The model parameters are achieved by the experiment results of the NiTi (50.8% Ni) wires conducted by Soul and Yawny (2017). The austenitic modulus is 50GPa, the phase transformation starting stress is 262MPa, α and β shown in Fig. 1(c) are 0.0234 and 0.668, respectively.

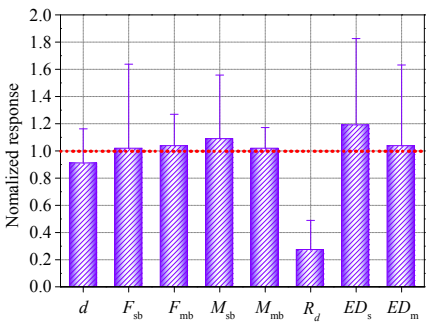

Fig. 5. Mean values and standard deviations of normalized responses

Fig. 5 shows the mean values and standard deviations of normalized responses of the sliding-LRB system with SMA devices. It can be observed that the mean residual displacement (R_d) shows a 73.1% reduction, and the mean peak displacement (d)

shows a 9.3% reduction. This is because the superelsticity and flag-shape hysteretic behavior of the SMA devices provide reliable re-centering and energy dissipation capabilities. Since more amount of SMA wires are used in side bearings, the contribution of the SMA devices for the energy dissipation of the side bearing (ED_s) is relatively larger than the middle bearings and reaches 18.9%, whereas the contribution for that of the middle bearing (ED_m) is much less. Meanwhile, the base shear (F_{sb}, F_{mb}) and bending moment (M_{sb}, M_{mb}) of the piers show a maximum increase of 8.6%. This is because adding SMA devices can increase the stiffness of the sliding-LRB system, whereas the increment in base forces of the piers is slightly due to its lower elastic modulus after yielding. Overall, the above results shown that adding the SMA device into the sliding-LRB system can effectively reduce the residual displacement and improve the energy dissipation capability of the sliding-LRB system. However, it leads to a slight increase in the base forces of the piers.

4. CONCLUSIONS

In the present study, adding SMA devices into the sliding-LRB system can effectively reduce the residual displacement and improve the energy dissipation of the system. whereas only lead to a slightly increase in base forces of the piers. This study adopts an idealized flag-shape model for the SMA devices. It is needed to investigate the performance of the SMA devices using an improved SMA model with temperature effect and rate dependency in future study. Moreover, the SMA devices can be replaced when the damage occurred to it after a serious earthquake event.

ACKNOWLEDGEMENTS

The first two authors would like to acknowledge the finacial support from the National Natural Science Foundation of China (No. 51578151), the National Scholarship Fund of China Scholarship Council (201806090090) and Curtin University.

REFERENCES

American Society of Civil Engineers (ASCE). (2005) Minimum design loads for buildings and other structures, Standard ASCE/SEI 7-05, Reston, VA.

Andrawes, B., and DesRoches, R. (2007) Comparison between shape memory alloy seismic restrainers and other bridge retrofit devices, Journal of Bridge Engineering Vol 12, No 6, pp 700-709.

Bi, K., Hao, H., and Chouw, N. (2013) 3D FEM analysis of pounding response of bridge structures at a canyon site to spatially varying ground motions, Advances in Structural Engineering Vol 16, No 4, pp 619-640.

Cardone, D., and Gesualdi, G. (2017) Influence of residual displacements on the design displacement of spherical friction-based isolation systems, Soil Dynamics and Earthquake Engineering Vol 100, pp 492-503.

Constantinou, M. C., and Adnane, M. A. (1987) Dynamics of soil-base-isolated structure systems: evaluation of two models for yielding systems. Report to NSAF, Department of Civil Engineering, Drexel University, Philadelphia.

Constantinou, M., Mokha, A., and Reinhorn, A. (1990) Teflon bearings in base isolation II: Modeling, Journal of Structural Engineering Vol 116, No 2, pp 455-474.

Dezfuli, F. H., and Alam, M. S. (2013) Shape memory alloy wire-based smart natural rubber bearing, Smart Materials and Structures Vol 22, No 4, pp 045013.

Dolce, M., Cardone, D., and Croatto, F. (2005) Frictional behavior of steel-PTFE interfaces for seismic isolation, Bulletin of Earthquake Engineering Vol 3, No 1, pp 75-99.

Günay, M. S., and Sucuoğlu, H. (2009) Predicting the seismic response of capacity-designed structures by equivalent linearization, Journal of Earthquake Engineering Vol 13, No 5, pp 623-649.
Kalpakidis, I. V., Constantinou, M. C., and Whittaker, A. S. (2010) Modeling strength degradation in lead-rubber bearings under earthquake shaking, Earthquake Engineering & Structural Dynamics Vol 39, No 13, pp 1533-1549.
Kromanis, R., Kripakaran, P., and Harvey, B. (2016) Long-term structural health monitoring of the Cleddau bridge: evaluation of quasi-static temperature effects on bearing movements, Structure and Infrastructure Engineering Vol 12, No 10, pp 1342-1355.
Li, C., Hao, H., and Bi, K. (2017) Numerical study on the seismic performance of precast segmental concrete columns under cyclic loading. Engineering Structures, Vol 148, pp 373-386.
Loh, C. H., Liao, W. I., and Chai, J. F. (2002) Effect of near-fault earthquake on bridges: lessons learned from Chi-Chi earthquake, Earthquake Engineering and Engineering Vibration Vol 1, No 1, pp 86-93.
Ministry of Transport of PRC. (MTPRC). (2013) Friction pendulum seismic isolation bearing for highway bridges (JT/T 852-2013), China Communications Press, Beijing.
Ministry of Transport of PRC (MTPRC). (2008) Guidelines for seismic design of highway bridges (JTG/T B02-01-2008). China Communications Press, Standard MTPRC, Beijing.
Moorty, S., and Roeder, C. W. (1992) Temperature-dependent bridge movements, Journal of Structural Engineering Vol 118, No 4, pp 1090-1105.
Otsuka, K., and Wayman, C. M. (1999). Shape memory materials, Cambridge university press.
Ozbulut, O. E., and Hurlebaus, S. (2011) Optimal design of superelastic-friction base isolators for seismic protection of highway bridges against near-field earthquakes, Earthquake Engineering & Structural Dynamics Vol 40, No 3, pp 273-291.
Pacific Earthquake Engineering Research Center (PEERC). (2016) OpenSees-Version 2.5.0, Open System for Earthquake Engineering Simulation, Berkeley.
Somerville, P. G., Smith, N. F., Graves, R. W., and Abrahamson, N. A. (1997) Modification of empirical strong ground motion attenuation relations to include the amplitude and duration effects of rupture directivity, Seismological Research Letters Vol 68, No 1, pp 199-222.
Soul, H., and Yawny, A. (2017) Applicability of superelastic materials in seismic protection systems: a parametric study of performance in isolation of structures, Smart Materials and Structures Vol 26, No 8, pp 085036.
Wang, H., Zheng, W. Z., Li, J., and Gao, Y. Q. (2019) Effects of temperature and lead core heating on response of seismically isolated bridges under near-fault excitations, Advances in Structural Engineering Vol 22, No 14, pp 2966-2981.
Wilson, J. C., and Wesolowsky, M. J. (2005) Shape memory alloys for seismic response modification: a state-of-the-art review, Earthquake Spectra Vol 21, No 2, pp 569-601.
Xing, C. X., Wang, H., Li, A. Q., and Wu, J. R. (2012) Design and experimental verification of a new multi-functional bridge seismic isolation bearing, Journal of Zhejiang University Science A Vol 13 No 12, pp 904-914.
Zhang, Y., and Zhu, S. (2007) A shape memory alloy-based reusable hysteretic damper for seismic hazard mitigation, Smart Materials and Structures Vol 16, No 5, pp 1603.
Zheng, W. Z., Wang, H., Li, J., and Shen, H. J. (2019) Parametric study of SMA-based friction pendulum system for response control of bridges under near-fault ground motions, Journal of Earthquake Engineering, pp 1-19.